UNIVERSITY OF CALIFORNIA, SAN DIEGO

Mechanisms of cross-shore transport in the inner shelf, off the coast of central Point Loma

A Thesis submitted in partial satisfaction of the requirements for the degree Master of Science

in

Engineering Sciences (Aerospace Engineering)

by

Ajinkya Desai

Committee in charge:

Professor Eugene Pawlak, Chair
Professor Ed Parnell
Professor Sutanu Sarkar

2015

The Thesis of Ajinkya Desai is approved, and it is acceptable in quality and form for publication on microfilm and electronically:

_____

_____

_____

Chair

University of California, San Diego

2015

TABLE OF CONTENTS

LIST OF FIGURES

LIST OF TABLES

ACKNOWLEDGEMENTS

I would like to acknowledge Dr. Eugene Pawlak for his support as the Chair of my Committee. His continuous guidance and frequent insights have been very helpful.

I would also like to acknowledge Dr. Ed Parnell, from the Scripps Institute of Oceanography, for providing the data used in this research and his frequent insights that have been very helpful.

Chapters 1, 2 and 3, each in part, are currently being prepared for submission for publication of the material. Desai A.; Pawlak E.; Parnell E. The thesis author was the primary investigator and author of this material.

ABSTRACT OF THE THESIS

Mechanisms of cross-shore transport in the inner shelf, off the coast of central Point Loma

by

Ajinkya Desai

Master of Science in Engineering Sciences (Aerospace Engineering)

University of California, San Diego, 2015

Professor Eugene Pawlak, Chair

This main objective of this study is to identify and estimate the contribution of various forcing mechanisms that drive cross-shore exchange in the inner shelf, off the coast of central Point Loma. Analysis of the structure of velocity profile time series recorded by a bottom-mounted ADCP indicates that internal tides are the dominant mechanism contributing to cross-shore exchange on the inner-shelf. Exchange is predominantly manifested via a two-layered exchange mode. Much of the variability explained by this mode is associated with the M_2 internal tide. The total M_2 energy is found to be stronger beneath the thermocline for most of the year. The vertical asymmetry of the M_2 is accounted for by the phase relationship between the barotropic and baroclinic M_2 tide. Seasonal shifts in the depth of the thermocline determine the vertical extent of the baroclinic M_2 in the lower layer. The exchange flux driven by the M_2 accounts for

approximately 35% of the net cross-shore exchange flux. Variability in diurnal processes is relatively weaker. It is mostly accounted for by semi-diurnal and diurnal internal tides in the summer.

Introduction

Coastal transport processes are vital to the provision of nutrients to giant kelp forests (*Macrocystis pyrifera*) off the coast of Point Loma peninsular. Cross-shelf fluxes are critical for the import of nutrients and pollutants nearshore, which impacts ecological and human health. Cross-shore flow also affects water quality in the region surrounding the Point Loma ocean outfall (PLOO). A report (Shaffer et al., 2007) submitted to the wastewater department of San Diego acknowledges the complexity of the oceanographic conditions in this region and the need for further study regarding the shoreward transport of effluent discharged in the PLOO area.

Several forcing mechanisms that drive cross-shore flow have been the focus of previous analyses of oceanographic data. These mechanisms depend on the local bathymetry, offshore stratification and meteorological conditions. In a fringing coral reef on the south shore of Oahu, thermally driven baroclinic exchange was found to be the dominant mechanism for cross-shore transport (Molina et al., 2014). In the inner shelf of Monterey Bay, cross-shelf exchange was found to be driven mainly by alongshore winds and episodic roles played by surface gravity waves during periods of weak upwelling (Woodson, 2013). Cross-shelf winds drive a two-layer exchange in the inner continental shelf, off the south shore of Martha's Vineyard (Fewings et al., 2008). Off of Mission beach, semi-diurnal internal tides were found to dominate cross-shore flow in the shelf-break region and narrow shelf, which were more energetic on the latter (Lerczak et al., 2003). Seasonal stratification assumes importance in the study of cross-shore nutrient transport driven by internal tidal bores. Analysis of dissolved inorganic nitrate (DIN), in the Santa Barbara channel (McPhee-Shaw et al., 2007) showed that nutrient supply mechanisms vary seasonally. These include diurnal internal waves in the summer (when stratification is strong) and upwelling in late fall and early winter. A study by Lucas et al. (2011) revealed that semi-diurnal internal tides are the primary source of nitrate fluxes in the inner shelf of the Southern California Bight (SCB). Their

analysis suggests that much of the nitrate budget is controlled by nitrate fluxes in the sub-thermocline layer, which further control biological productivity in the inner shelf. Vertical motion of the thermocline, associated with the semidiurnal internal tide and internal waves, is known to account for the distribution of nitrates (Cullen et al., 1983).

This study examines the contribution of key mechanisms that drive cross-shore exchange off central Point Loma. These mechanisms are active at different time scales. The observations and results presented imply that most of the variability in the cross-shore exchange flow here is regulated by the M_2 internal tide. Preliminary observations and data are presented in section 1. The primary structure of cross-shore exchange and its driving mechanisms are analyzed in section 2 with particular emphasis on the vertical structure of the M_2 tide. Relative contributions of internal waves to the exchange, at semi-diurnal and diurnal frequencies, have been estimated and discussed in section 3.

Chapter 1. Background and Observations

1.1. Measurement Sites

A bottom mounted acoustic Doppler current profiler (ADCP) and thermistor chain (T-chain) were used to collect data at a 33m isobath, approximately 1.85 km off the west coast of the Point Loma peninsula, just offshore of one of the largest kelp forests in Southern California (Jackson, 1984). The ADCP (600 kHz RDI Workhorse) sampled velocity every 5 minutes between 8m and 31m within 2m vertical bins. Temperature sensors (TidbiT Temperature Data Logger), spaced by 4m, recorded observations every 10 minutes between 3m and 30m depths. Wind speed and direction were obtained from NOAA archives of data recorded hourly, at the Naval Outlying Landing Field, located about 21 km southeast of the 33m station, on Imperial Beach. Wave data is taken from Coastal Data Information Program (CDIP) archives for a point located 23 km to the southwest of the deployment.

The analysis presented here is for the year 2013. ADCP data were available in two parts from (i) late January to mid-June and (ii) mid-July to December. Temperature sensors collected data all year but were replaced in March and August. Offsets were introduced in the temperature signal at some depths as a side-effect of the replacement. These were corrected by linear extrapolation of signals at neighboring depths.

Figure 1 shows an aerial view of the bathymetric contours around the location of the bottom mounted ADCP and T-chain. The local bathymetry around the deployment is relatively irregular, making definition of cross and along-shore directions indefinite. The cross and along-shore velocity components are obtained by rotating the currents into a coordinate system aligned with the axis of principal variance in the depth-averaged currents. The alongshore direction is aligned approximately 15° clockwise from the true North. The cross-shore component is positive onshore and the alongshore component is positive in the North-North West direction.

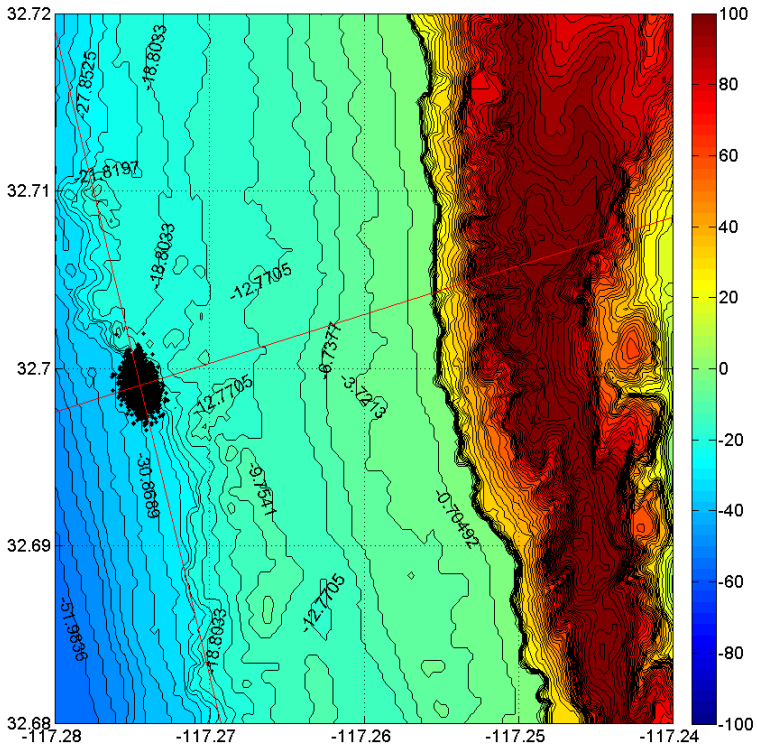

Figure 1. Bathymetry for the west coast shore of Point Loma peninsular including the 33m deployment and 33m thermistor chain with the depth-averaged cross-shore, alongshore velocities and principal axes.

1.2. Data Overview

The cross-shore exchange velocity is defined by subtracting depth-averaged velocity from the cross-shore velocity ($V_y(z)$) measurements at each depth. The contribution due to depth-averaged flux and exchange flux is obtained as

$$\Gamma_m = \int_{-h}^{0} \bar{V}_y dz \qquad (1)$$

$$\Gamma_{ex} = \frac{1}{2} \int_{-h}^{0} |V_y(z) - \bar{V}_y| dz \qquad (2)$$

where h is the deployment depth, $\bar{V}_y$ is the depth-averaged cross-shore velocity, Γ_m is the mean flux and Γ_{ex} is the exchange flux.

The cross-shore fluxes, meteorological and T-chain data are summarized in Figure 2. The daily pattern of the cross-shore wind in Figure 2a shows on-shore winds from late morning and early afternoon, throughout 2013. Winds that prevail for the rest of the day carry a seasonal signature. They are relatively weak from March to September and strongly off-shore in the remaining months of the year. The diurnal wind pattern also has a southward alongshore component throughout most of the year (Figure 2b), with intermittent periods of southerly (downwelling) winds, particularly in late spring.

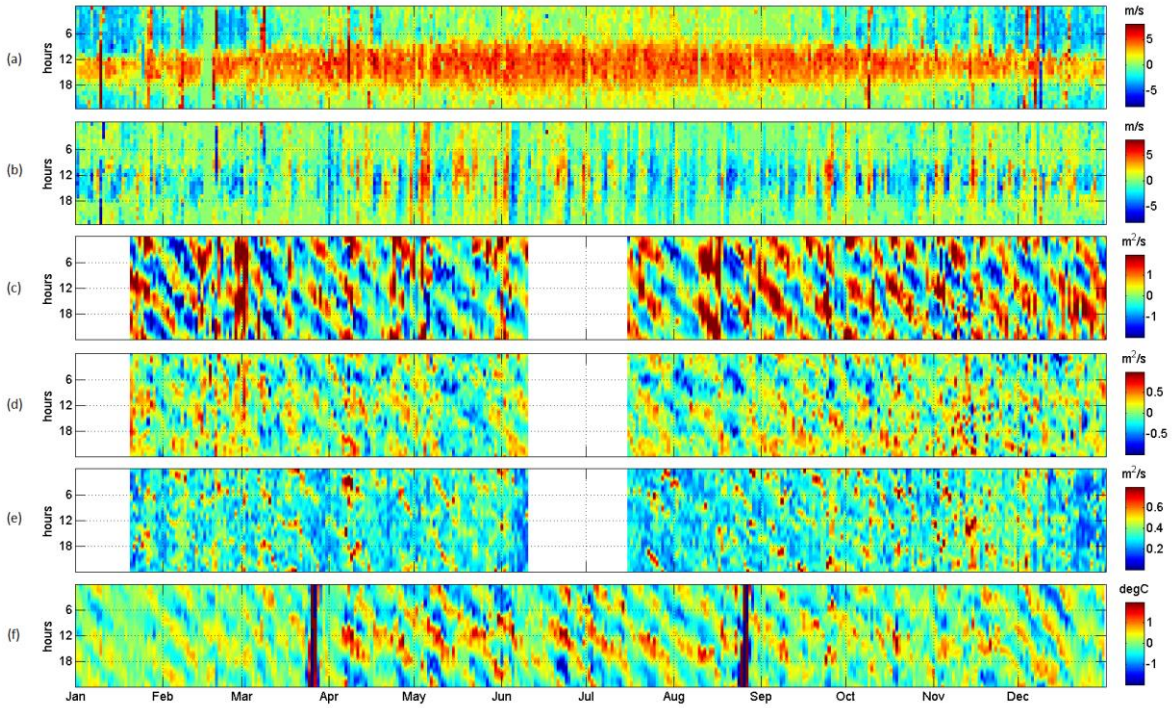

Figure 2. Summary of observations at central Point Loma for 2013. Time of year on horizontal axis and hour of day on vertical axis. (a) cross-shore wind velocity (+ onshore) (b) alongshore wind velocity (+NNW) (c) alongshore depth-averaged water flux (+NNW) (d) cross-shore depth-averaged water flux (+onshore) (e) cross-shore exchange water flux (f) high-pass filtered (66 h) depth-averaged water temperature.

Figure 2d and 2e are annual plots of the cross-shore mean and exchange flux versus time of the day. As is evident in the diagonal banding in both panels, both mean and exchange fluxes are predominantly driven by the semidiurnal M_2 tide. Some variability associated with the diurnal frequency is indicated by horizontal banding. Diagonal banding in the alongshore mean flux

(Figure 2c) is also associated with the semidiurnal M_2 tide. As expected, the M_2 is stronger in the alongshore mean flux as compared to that in than in the cross-shore mean flux.

The high-pass filtered (66 h cut off), depth averaged temperature is shown in figure 2f for 2013 versus time of day. The diagonal banding indicates that the high-frequency component of temperature responds to the M_2 tide. The M_2 intensity increases between March and August, when stratification is stronger. This indicates that the M_2 is likely associated with internal tides, suggesting a baroclinic influence. There is some variability at the diurnal frequency, particularly in the months from September to December.

Low-pass filtered (66 h cut-off) temperature (T_{LP}) is shown in figure 3 to illustrate the seasonal variability in temperature and stratification over 2013. Stratification is relatively weak from November to February. Frequent spells of upwelling are observed in the months from April to August. This is when the near-surface temperature falls below its seasonal mean of 15°C. Cool water is drawn from the ocean into the inner shelf at depth and up to the surface.

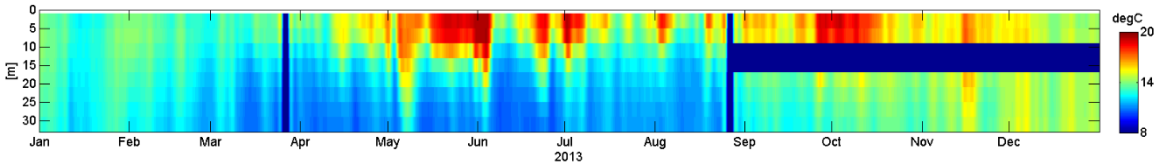

Figure 3. Low-pass filtered (66 h) water temperature profile for 2013 data versus depth.

Significant wave heights (H_s) at the location of the deployment have been presented in Figure 4. Wave heights at the 33m station are estimated by conserving the wave energy flux between the CDIP and the 33m stations. These are relatively higher in the months of January to early April, associated with intermittent winter storms.

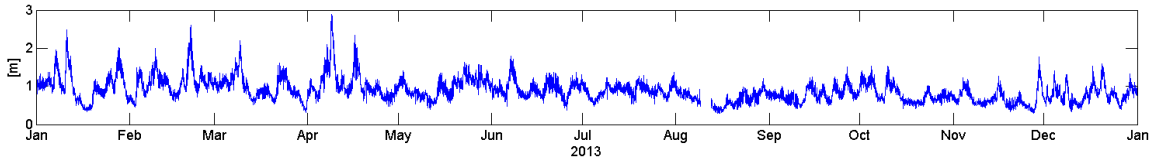

Figure 4. Shallow water significant wave heights for 2013.

1.3. Frequency Spectrum

The variance associated with relevant time scales is determined from estimates of the variance-preserving spectra for the cross-shore fluxes (Figure 5a). For the cross-shore exchange flux, a large peak is observed at the M_2 frequency (1.93 cpd), which accounts for most of the variance in the spectral energy. There are relatively smaller peaks at diurnal frequency (1 cpd), S_2 (2 cpd) and at higher harmonics. The M_2 signal also contributes to the peak at the M_4 frequency, since the period of the M_2 signal doubles when the absolute value of the exchange velocity is taken in equation 2. However, the M_2 persists due to the influence of a low frequency exchange profile. A steady exchange combined with a pure M_2 exchange will lead to an asymmetric (positive) semidiurnal exchange. This will produce a zero frequency component, M_2, M_4 and higher harmonics. For the depth-averaged flux, there is a large peak at the M_2 frequency that accounts for most of the variance in the spectral energy. There is a peak at the diurnal frequency as well.

1.4. Diurnal Flow Pattern

The vertical structures of the diurnal flow and temperature profiles are presented in Figures 6 and 7. ADCP and T-chain data are averaged with time of day in two parts (i) April to September for summer and (ii) October to March for winter. Temperature signals are anomalies from the depth-averaged low pass filtered (66 h cut off) temperature ($\overline{T}_{LP}$). The diurnal alongshore flow in both seasons (Figures 6b, 7b) reveals a barotropic structure influenced by the semi-diurnal S_2 tide. Remarkable differences are observed in the cross-shore diurnal flow patterns of both seasons. The winter diurnal cross-shore flow (Figure 7d) is characterized by distinct three-layer baroclinic

patterns that pervade throughout the day. In the summer (Figure 6d), the near-surface off-shore flow and on-shore flow at depth, in the afternoon, is suggestive of a heating cycle, while the offshore flow at depth and near-surface onshore flow post mid-night, suggests a possible cooling cycle. The water temperature profile in summer (Figure 6f) indicates a clear diurnal pattern and peaks in the afternoon hours. There is a phase difference between peak temperatures at different depths, showing an upward propagation of phase that is not observed in the winter temperature profile (Figure 7f).

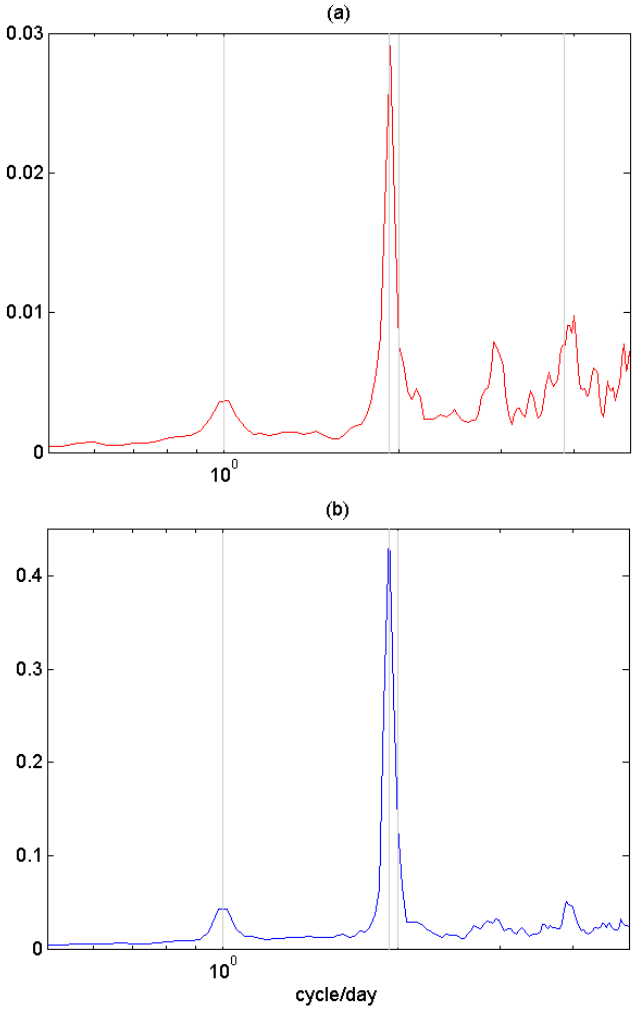

Figure 5. Variance-preserving spectrum for (a) cross-shore exchange flux (red), (b) cross-shore depth-averaged flux (blue) for 2013.

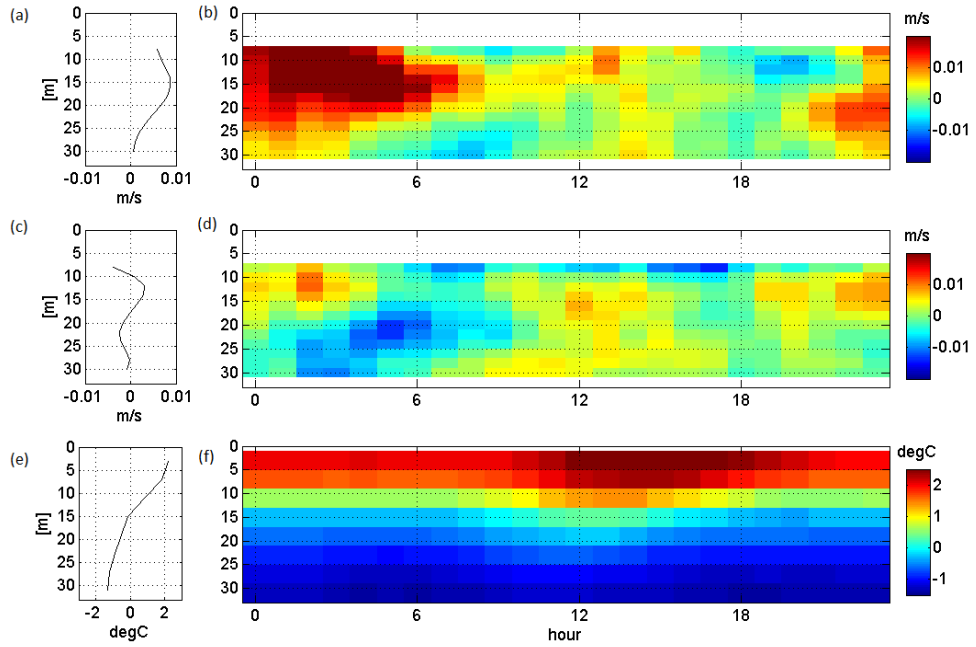

Figure 6. Time-averaged profile and variation with time of day, each versus depth, of summer (Apr-Sep) data set for (a, b) alongshore velocity (c, d) cross-shore velocity (e, f) temperature relative to depth-averaged low-pass (66 h) filtered temperature.

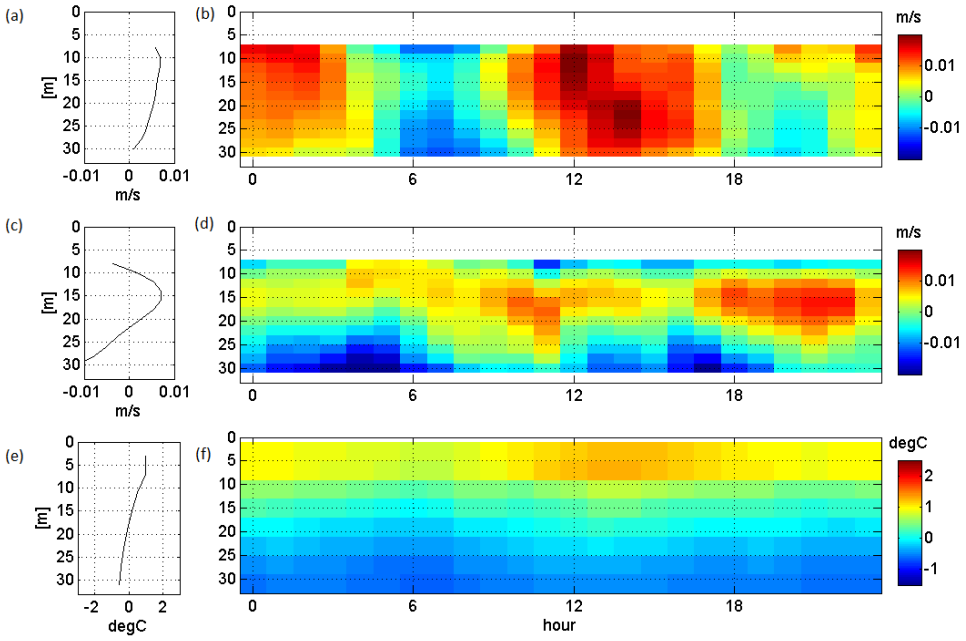

Figure 7. Time-averaged profile and variation with time of day, each versus depth, of winter (Oct-Mar) data set for (a, b) alongshore velocity (c, d) cross-shore velocity (e, f) temperature relative to depth-averaged low-pass (66 h) filtered temperature.

Average diurnal patterns for the flow and forcing are summarized in figure 8. The cross-shore wind is onshore with maximum amplitude in the afternoon and offshore for the rest of the day. It must be noted that the near-surface off-shore flow in the afternoon, for both seasons (Figures 6d, 7d), is inconsistent with diurnal wind forcing. This suggests that the influence of diurnal wind stress on the cross-shore flow is not high.

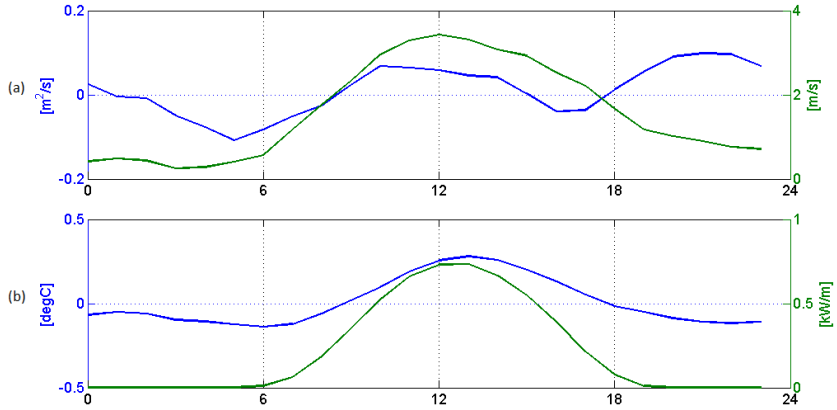

Figure 8. Diurnal variations of (a) depth-averaged cross-shore flux (blue), cross-shore wind velocity (green) for 2013. (b) Depth-averaged high-pass filtered (66 h) temperature (blue), solar irradiance (green) for 2013.

Interpretation of the diurnal depth-averaged temperature pattern (Figure 8b) requires background from a previous study (Molina et al., 2014). The dynamics of thermally-driven cross-shore exchange is governed by the buoyancy equation (equation 4, Molina et al., 2014), which balances unsteady and advective terms with forcing buoyancy flux at the surface and thermal diffusion. Phase relationships between the forcing flux and temperature response inform the dominance of either the advective terms or unsteady terms. In the unsteady regime, the temperature lags the forcing by 90°. In the advective regime, temperature is in phase with the surface heat flux. In this study, solar irradiance (obtained from a rotating shadow-band radiometer at Loyola Marymount University, Los Angeles) is used as a surrogate for surface heat flux. Although the solar irradiance data was obtained quite far from the location of the deployment, it is

useful for a general perspective. The depth-averaged temperature and solar irradiance are in phase (Figure 8b). This implies that the thermal response to surface heat flux lies in the advective regime, unless it is determined by internal wave forcing, which is discussed later. Remarks on thermal exchange flux are mentioned in the next chapter.

Chapter 1, in part, is currently being prepared for submission for publication of the material. Desai A.; Pawlak E.; Parnell E. The thesis author was the primary investigator and author of this material.

Chapter 2. Analysis

2.1. Relative contribution of exchange flow

The importance of the cross-shore exchange flux relative to the depth-averaged (mean) flux is estimated here. Low-pass filtered (3 h cut off) fluxes shown in figure 9, indicate that variability in the mean flux is much higher than that in the exchange flux. However, the exchange flux exceeds the mean flux 40% of the time in 2013. The annual average of Γ_{ex} is calculated to be 0.3404 $m^2 s^{-1}$, while that of Γ_m is 0.4268 $m^2 s^{-1}$. These average fluxes can be interpreted in terms of an average cross-shore 'flushing' time. This represents an estimate of the time required for the cross-shore flow to replace the region inshore of the deployment site. Average flushing timescales are estimated using a procedure similar to the one outlined in Molina et al. (2014). The inshore region can be idealized as a 1.85 km × 33 m wedge. The average time scale for nearshore flushing due to the exchange is V/Γ where Γ is the time-averaged volume flux and V is the volume (per unit alongshore distance) of the nearshore region.

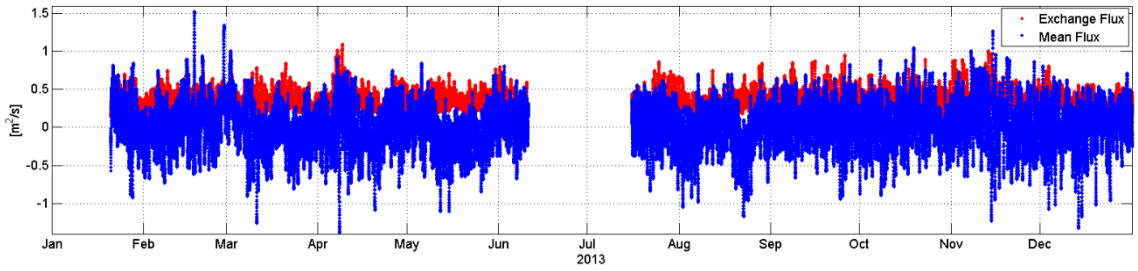

Figure 9. Low-pass filtered (3 h) cross-shore volume flux estimates for 2013 due to depth-averaged flow (blue) and exchange (red).

The average flushing time scales for flushing the wedge, associated with the mean flux and exchange flux are about 20 h and 24 h, respectively. Although this procedure indicates that the average exchange flux is smaller than the average mean flux, these flushing time scales are not radically different. The exchange flux remains important in determining the residence time of nutrients inshore. The mean and exchange fluxes are hypothesized to play different roles in nutrient

transport on the inner shelf. The mean flux assists in transporting nutrients to and forth from the kelp forest. The flux due to exchange is known to assist the vertical distribution of nutrients at the kelp forest (Rosman et al., 2007).

2.2. Predominant modes of exchange

An empirical orthogonal function analysis is carried out on the time series of the cross-shore exchange velocity profiles to identify the dominant modes that make up the vertical structure of cross-shore exchange flow. This was done using MATLAB's EOF function that performs a singular value decomposition on the hourly profile time series. The first mode (figure 10a) accounts for about 65% of the total variance in the cross-shore exchange. It captures a two-layered exchange profile and appears to be strongly sheared at the thermocline. The second mode (figure 10b) accounts for 18% of the variance and represents a three-layered exchange flow. The higher variance associated with the first mode indicates that most of the energy in the M_2 exchange velocity is invested in a two-layered exchange mode. The first mode also captures much of the diurnal variability in the exchange flow. The variance associated with the diurnal frequency in the first mode is 20% of the variance associated with the M_2 frequency in the first mode, as obtained from the spectrum of this mode.

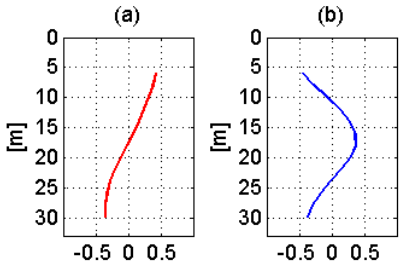

Figure 10. EOF modes of the cross-shore exchange velocity profile for 2013. Modal amplitude versus depth for (a) first mode (b) second mode.

2.3. Forcing mechanisms for cross-shore transport

2.3.1. M_2 Tide

The cross-shore velocity signal at each depth is demodulated at the M_2 tidal period (12.42 h) using a 14 day running window. The amplitude and phase are calculated using a least-squares fit. The vertical structure and seasonal changes in the M_2 profile are shown in Figure 11a for 2013, as calculated from the complex demodulation. The amplitude of the M_2 is much higher at depths below 15m. The strength of the M_2 appears to be relatively uniform over the year. The influence of the M_2 is confined near the bed in the winter months (October-March) while it stretches to shallower depths in the summer months (April-September). Phase estimates, computed relative to the midnight of 1/21/2013 are plotted in Figure 11b, for reference. A similar demodulation process is used to synthesize the depth-averaged M_2 tidal velocity from the depth-averaged cross-shore velocity. The complex result is identified here as the barotropic M_2 component.

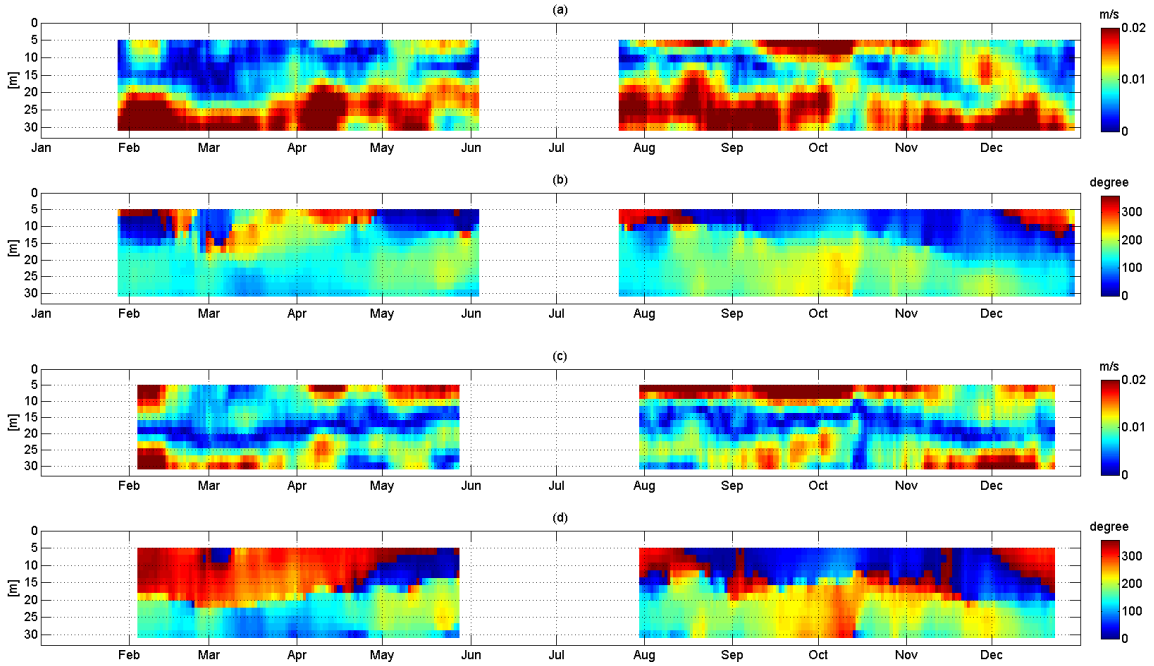

Figure 11. (a) Amplitude of demodulated cross-shore velocity profile at M_2 tidal period (12.42 h) for 2013 versus depth (b) slowly-varying phase of M_2 velocity profile, relative to 1/21/2013 midnight, versus depth. (c) Amplitude of cross-shore baroclinic M_2 velocity profile for 2013 versus depth (d) slowly-varying phase of baroclinic M_2 profile, relative to 1/21/2013 midnight, versus depth.

The resultant velocity profile obtained after subtracting the barotropic M_2 velocity from the cross-shore velocity is also demodulated to obtain the baroclinic M_2 profile. Figure 11c shows the baroclinic amplitude versus depth and time of year. The amplitude of the baroclinic M_2 is high at depths near the surface and near the bed, and relatively lower at water depths in between. This is consistent with the two-layer exchange flow mentioned in section 2.2. The region of low amplitude shifts to shallower depth in April to September and deeper from October to March. The vertical phase structure of the baroclinic M_2 (Figure 11d) shows attributes of the two-layer exchange profile for most of the year. The phase changes sharply at the depth of zero-crossing from the top layer to the bottom layer, so that they are 180° out of phase. This indicates that the phase is likely related to the direction of flow in each layer.

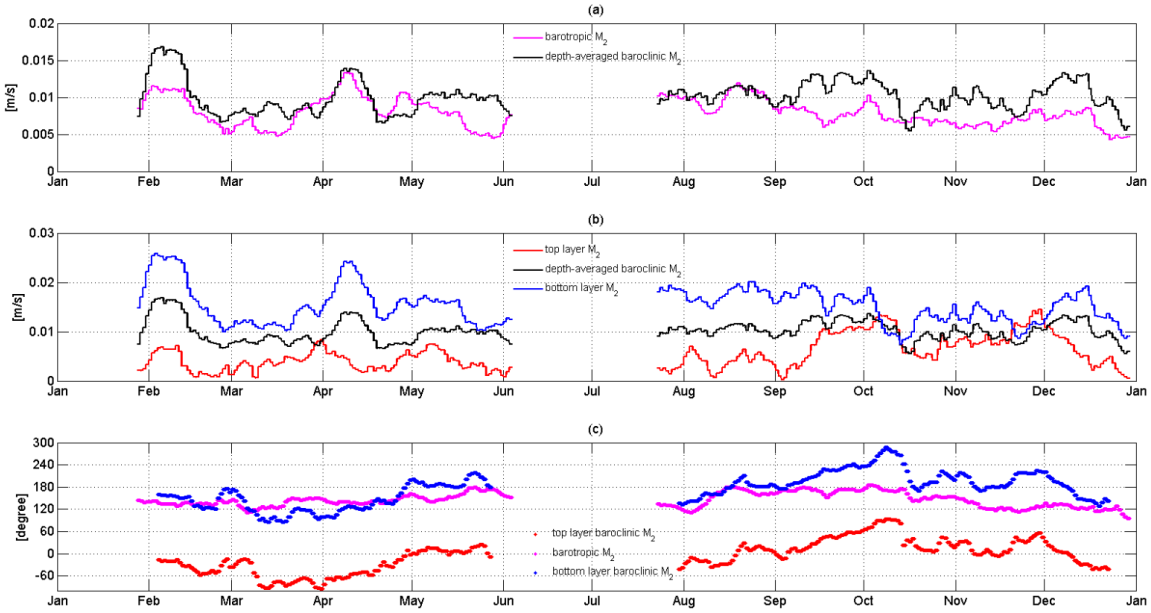

Figure 12. (a) Amplitude of barotropic M_2 (pink), depth-average of the baroclinic M_2 amplitude (black), (b) amplitude of top-layer M_2 tide (red), amplitude of bottom-layer M_2 tide (blue), depth-average of baroclinic M_2 amplitude (black), (c) phase of barotropic M_2 (pink), phase of top-layer baroclinic M_2 (red), phase of bottom-layer M_2 (blue).

To explore the asymmetric nature of the M_2 velocity, the cross-shore velocity time series, depth-averaged separately over the top layer (8-18m depth) and the bottom layer (20-30m depth),

are demodulated at the M_2 frequency. The baroclinic M_2 amplitude is obtained from the depth average of the baroclinic M_2 shown in Figure 11c. This is plotted along with the barotropic M_2 in Figure 12a. The depth-averaged baroclinic M_2 amplitude and the barotropic M_2 amplitude (β_{M_2}) are quite similar in magnitude, over 2013. The annual average of the M_2 amplitude in the bottom layer (B_{M_2}) is more than twice the annual average of the M_2 amplitude in the top layer (T_{M_2}). Exceptions to this bottom-layer intensified M_2 tide are seen in early October and late November, when B_{M_2} decreases and T_{M_2}increases to beyond the former (Figure 12b).

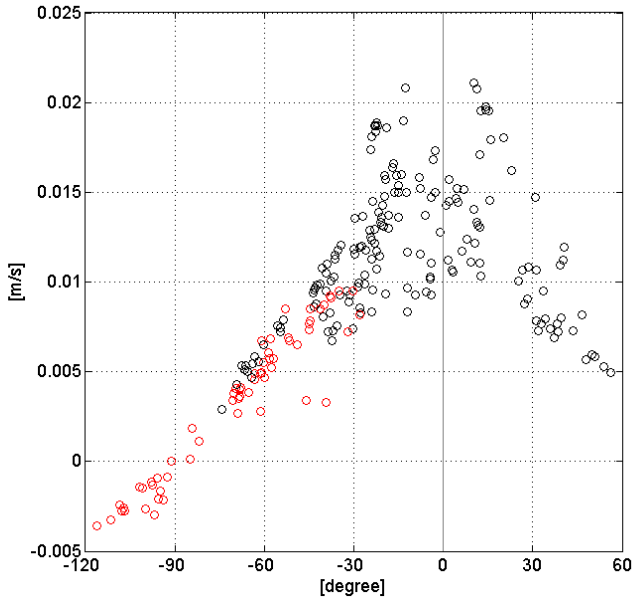

Figure 13. Difference in the amplitudes of bottom-layer M_2 and top-layer M_2 tidal signals plotted versus the difference in phase of barotropic M_2 and bottom-layer baroclinic M_2 signals over 2013. Data points in the fall months of Oct-Dec in red.

The relative difference in M_2 amplitudes of the top and bottom layer is related to the phase difference of their respective baroclinic counterparts from that of the barotropic M_2 (Figure 12c). This is more readily apparent comparing the phase difference between the bottom-layer baroclinic M_2 and the barotropic M_2 signal on one hand and the difference in B_{M_2} and T_{M_2} time series on the

other (Figure 13). When the barotropic M_2 is in phase with the bottom-layer baroclinic M_2, they add constructively in the bottom layer. The addition is such that the flow is intensified at the bottom. This is the case for most of 2013. However, when they are in quadrature (90° out of phase), the barotropic M_2 signal adds constructively with the baroclinic M_2 signal in both layers. This addition is such that the total M_2 in the top layer increases and that in the bottom layer decreases, so that there is no vertical asymmetry in the total M_2 tide. This happens noticeably in the fall when T_{M_2}, averaged from October to November, is much higher than it is for the rest of the year.

2.3.2. Diurnal Internal Waves

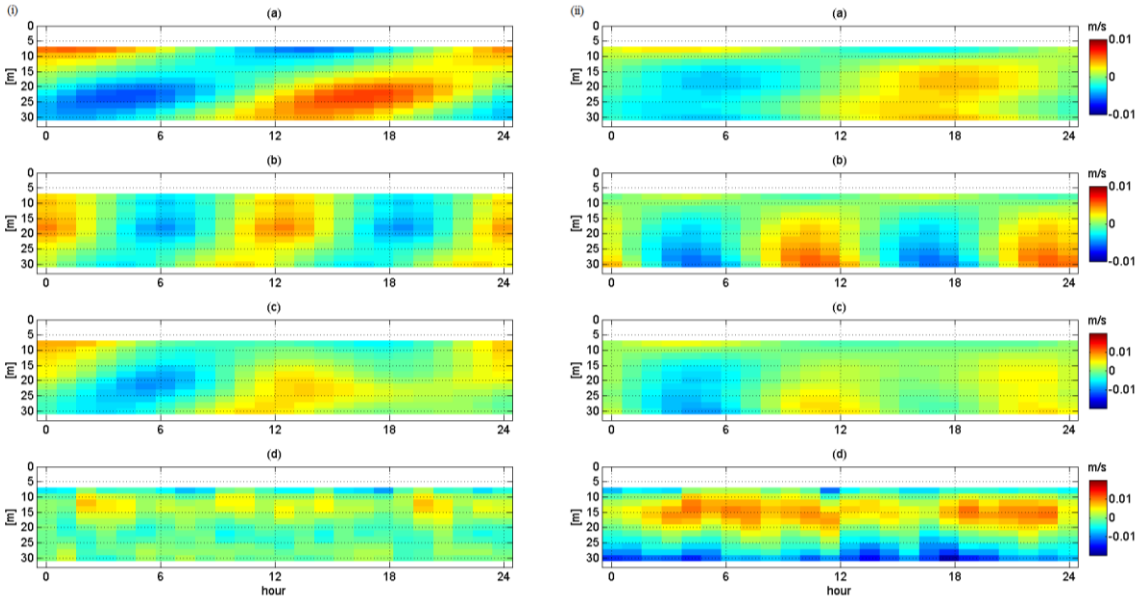

Figure 14. Averages with time of day versus depth for demodulated cross-shore velocity in (i) summer (ii) winter at (a) 1 cpd, (b) 2 cpd and (c) the sum of the averages at 1 cpd and 2 cpd, (d) residual left after subtracting (c) from the total cross-shore diurnal velocity profile.

The velocity record is also demodulated at the frequencies of the S_2, O_1 (0.93 cpd) and at 1 cpd. The demodulated signal at 1cpd includes the response to forcing by diurnal wind, surface heat flux and the K_1 tide. To analyze the source of variability in the diurnal cross-shore flow structure, diurnal averages at the S_2 and K_1 frequencies are computed (Figure 14) separately for summer and winter. The summer diurnal structure (Figure 14(i)) is of particular interest.

Amplitudes of the 1 cpd signals are higher at depth. The phase of the 1 cpd peaks at shallower depths lags those of the peaks nearer to the bed. The phase of the S_2 shows a similar pattern at depth. The sum of the S_2 and 1 cpd structures (Figure 14(i)c) is found to contribute much of the variability in the diurnal flow structure for the summer, which is not the case for winter. At this stage, not much can be inferred from the winter diurnal pattern (Figure 14(ii)c).

2.3.3. Diurnal Wind

Cross-spectral coherence (γ) estimates can be used to quantify the effect of the cross-shore wind forcing. The cross-shore wind speed and water velocity signals at each depth, over the year, are each divided into 72 hour signals (n_{av} =105) to obtain cross-spectral coherence and phase estimates at a high 210 DOF. The highest coherence values are obtained at 1 cpd, indicating that the cross-shelf wind forcing primarily operates diurnally. At higher frequencies phase estimates are unstable. A longer time series would be required to obtain estimates of coherence at low frequencies. Similarly, a longer time series is required to obtain estimates of coherence between alongshore wind velocity and cross-shore water velocity at low frequencies and high DOF, to quantify the variance associated with wind-driven upwelling. Table 1 summarizes estimates of coherence at 1 cpd and select depths.

The upper and lower bounds for 95% confidence interval (Bendat et al., 2010) around the coherence estimate is evaluated using

$$\frac{\gamma^2}{1+2\varepsilon} \leq \gamma^2 \leq \frac{\gamma^2}{1-2\varepsilon} \qquad (3)$$

where

$$\varepsilon(\gamma^2) = \frac{1-\gamma^2}{\gamma}\sqrt{\frac{2}{n_{av}}} \qquad (4)$$

The influence of wind stress would be expected to be stronger near the surface. However, at 8m depth, $\gamma = 0.247$ and $\varepsilon(\gamma^2 = 0.061) = 0.52$ so that $1 - 2\varepsilon < 0$. The upper bound is therefore, undefined for $\gamma^2 = 0.061$, indicating a very wide confidence interval for γ^2 even at high degrees of freedom. Furthermore, the wind and water velocity (at 8m) are completely out of phase. The analysis suggests that the effect of cross-shore wind on inner shelf cross-shore circulation in this region is minimal. Limitations include the lack of wind data closer to the deployment and lack of ADCP data in the top 6m of the water column.

Table 1. Estimates of coherence between cross-shore velocity and cross-shore wind at 1 cpd.

Cross-shore velocity depth	Coherence (γ)	Bounds for 95% confidence interval	Phase (degree)
Depth-averaged	0.3432	[0.2625, 0.6368]	+75
8m	0.2470	[0.1725, not defined]	-170
16m	0.3763	[0.2948, 0.6183]	+82
24m	0.4771	[0.3966, 0.6415]	+45

2.3.4. Thermal Exchange

Temperature spectrum peaks at both 1 cpd and the M_2 frequency, indicating that the temperature responds to both semi-diurnal as well as diurnal forcing. Cross-shore advective heat transport per unit alongshore distance, associated with the diurnal exchange flow, is evaluated using

$$Q_{ex} = \rho c_p \int_{-h}^{0} \langle (V_y(z) - \bar{V}_y)(T(z) - \bar{T}_{LP}) \rangle \, dz \qquad (5)$$

where $\langle\ \rangle$ denotes average with time of day, c_p is the specific heat capacity of water and Q_{ex} refers to the diurnal flux of heat energy due to cross-shore exchange (Molina et al., 2014), integrated over the water column. The diurnal variation of Q_{ex} for the summer and winter months is compared in Figure 15. In the summer, there is a positive flux in the night hours followed by a more persistent negative flux that begins in the morning and lasts until late evening. The winter pattern is relatively

indistinct but with lesser variability. In the summer, the region inshore of the deployment loses heat at an average daily rate of 135 kW (per m alongshore) while in winter, it gains at 92 kW. These result in temperature gradients along isobaths, which might possibly drive a cross-shore flow, offshore in the summer and onshore in the winter. Temperature measurements inshore of the deployment would be helpful to obtain gradients for a detailed study of thermally driven exchange.

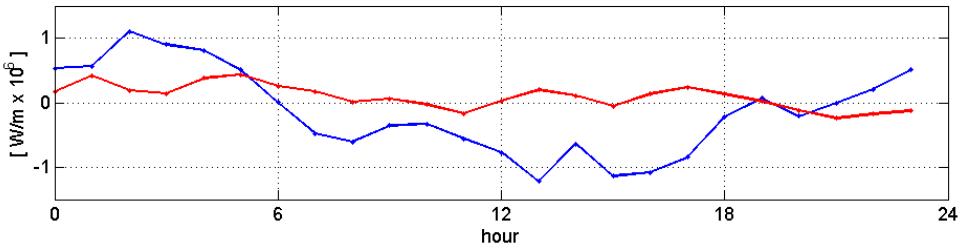

Figure 15. Q_{ex} in summer i.e. Apr-Sep (blue), in winter i.e. Oct-Mar (red) for 2013.

2.3.5. Stokes Drift

Flux due to Stokes drift is known to drive a return flow in the offshore direction on inner continental shelves (Lentz, 2008). Although this flow contributes to the mean flux, the above dynamic can be thought of as a mechanism for exchange of nutrients at the Stokes-Coriolis frequency (Lentz, 2012). The wave frequency is evaluated from T_p and the corresponding wave numbers (k_p) from the shallow water dispersion relation. The Stokes drift profile is evaluated from bulk parameters such as T_p and H_s using the following expression, as borrowed from Lentz et al. (2012),

$$u_{st}(z) = \frac{H_s^2 \omega k}{16} \frac{\cosh\big(2k(z+h)\big)}{\sinh^2 kh} \qquad (6)$$

The flux due to Stokes drift (Γ_{st}) is calculated by integrating equation 6 from the surface to the bed at the 33m station (Figure 16). It is found to be higher in the winter, from January to March, on account of larger wave heights. Comparison of the flux due to Stokes drift with the depth-averaged

cross-shore flux (Figure 9) indicates that its contribution is quite meagre. The offshore return flow driven by Stokes drift is found to contribute only about 12% of the mean flux over 2013. The higher waves in the winter months of January to March (Figure 13) contribute approximately 16 % of the mean flux in those months, which is slightly more than the contribution in the rest of the year.

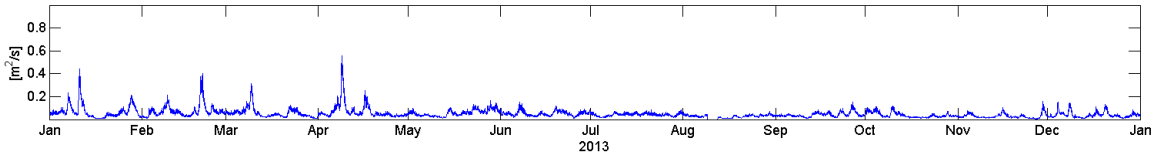

Figure 16. Cross-shore flux due to depth-integrated Stokes drift at peak period for 2013.

Chapter 2, in part, is currently being prepared for submission for publication of the material. Desai A.; Pawlak E.; Parnell E. The thesis author was the primary investigator and author of this material.

Chapter 3. Discussion

Most of the variability in the exchange flow is associated with the two-layered exchange flow structure depicted by the first EOF mode, which is predominantly driven by the M_2 tide. There is a relatively uniform phase difference of 180° between the top-layer M_2 and bottom-layer M_2 (Figure 12c). A similar observation was made by Lerczak et al. (2003) on the narrow shelf off of Mission Beach. For most of 2013, since the baroclinic top-layer M_2 is out of phase with the barotropic M_2, amplitude in the top layer is generally low and vice versa for the bottom layer. Exchange due to the baroclinic M_2 appears to be active throughout the year. In the fall, however, particularly when the top and bottom M_2 amplitudes approach each other in early October, the exchange is modified (Figure 11c). The M_2 component of the exchange flux is obtained from the M_2 exchange velocity profiles, where the depth-averaged velocity has been removed as in equation 2. A quantitative estimate of the M_2 contribution to the total cross-shore exchange flux is presented in table 2.

Table 2. Percentage estimates of the contribution of mechanisms active at different frequencies, to cross-shore exchange flux, as derived from demodulated cross-shore velocity profiles.

Frequency Band	Time period	Percentage of variance contributing to exchange Flux (14 day window)
Semi-diurnal	M_2 (12.42 h) Principal Lunar tide	35.54
	S_2 (12.00 h) Principal Solar tide	17.90
Diurnal	O_1 (25.82 h) Principal Lunar Diurnal tide	9.68
	(24 h) Wind / K_1 Luni-solar Tide	17.57

The M_2 tide appears to be strong beneath the thermocline and relatively much weaker in the mixed layer (Figure 11a). The thermocline level is shallower in the summer and deeper in the winter (Figure 11c). The height from the bed, up to which the influence of M_2 extends, changes accordingly. The bottom-layer intensified M_2 tide may have important implications in the transport of nutrients to the kelp forest. Nitrate concentration is usually higher below the thermocline where temperatures are generally low (Lucas et al., 2011). The strong M_2 at depth is very likely to deliver nitrates inshore for productivity of kelp. The possible influx of larvae by the internal tide (Pineda, 1999) is also likely to enhance suspension feeding along the kelp forest.

The diagonally banded structure of the response at the S_2 frequency in the summer (Figure 14(i)b), at depth, is likely associated with internal tides. High diurnal variability is seen at 1 cpd (Figure 14(i)a). Although this variability cannot be fully attributed to the K_1 since thermally driven exchange is also active at 1 cpd, the diagonal banding is strongly suggestive of a high internal tidal contribution. The inertial frequency at the location of study is 1.08 cpd. The K_1 is sub-inertial, so internal wave energy at 1 cpd can only persist as a coastally trapped evanescent flow response. Furthermore, the phase of these internal tides is seen to propagate towards the surface indicating that the energy propagates downward from the surface. A similar observation was made by Lerczak et al. (2001), who suggested that the source of energy is the diurnal wind. They further concluded that fluctuations in sub-tidal alongshore flow changes the local Coriolis parameter, making diurnal (1 cpd) motions operate at super-inertial frequencies. Although this could be linked to the high strength of the K_1 in the diurnal profiles, the downward propagation of energy remains unexplained. Since coherence of cross-shore wind with the cross-shore velocity is low (Table 1), a more comprehensive, rotary spectral analysis is required to examine whether the wind is the source of energy for internal tides. The diurnal temperature signals in the summer (Figure 6f) also respond to the internal tides, showing an upward propagation of phase. Hence, most of the diurnal

variability in the summer is attributed to K_1 and S_2 internal waves. The percentage contribution of thermally-driven exchange cannot be estimated at this stage.

As is consistent with previous analysis in the Southern California Bight (McPhee-Shaw et al., 2007), coastal upwelling in this region is weak and sporadic. Observations of the low pass filtered temperature (Figure 3), for the year 2013, show infrequent spells of upwelling limited to late spring and summer, from May to August. The effect of upwelling could be the vertical transport of nutrients to the surface, which would otherwise be nutrient-depleted due to high surface temperatures. A longer time series would be useful to obtain estimates of coherence between alongshore wind velocity and cross-shore water velocity at lower frequencies and high DOF, for a measure of the variance explained by Ekman transport in the inner-shelf circulation.

Future work in this region could focus on exploring the cause behind the phase relationship between the bottom-layer baroclinic M_2 and barotropic M_2. Analysis of a longer velocity time series could be helpful in determining the consistency of observations made over the year 2013. Similarly, the spatial structure of the M_2 can also be analyzed from data at different alongshore stations. Temperature measurements at stations inshore of the mooring could be useful in obtaining temperature gradients that drive baroclinic exchange in the inner shelf, so as to obtain a quantitative measure of their contribution to the cross-shore exchange in this region.

Chapter 3, in part, is currently being prepared for submission for publication of the material. Desai A.; Pawlak E.; Parnell E. The thesis author was the primary investigator and author of this material.

References

Bendat S.J., Piersol G. A., 2010, *Random Data: Analysis and Measurement Procedures*, Wiley, USA, 640 pp.

Coastal Data Information Program, 1999, Historic Wave Data- Point Loma South, CA, Scripps Institute of Oceanography, http://cdip/?&sub=data&nav=historic&stn=191&stream=p1 [9 Apr, 2015]

Emery J.W., Thomson E.R, 1998, *Data Analysis Methods in Physical Oceanography*, Pergamon, Great Britain, 634 pp.

Jackson G.A., 1984, Internal Wave Attenuation by Coastal Kelp Stands, *Journal of Physical Oceanography*, 14, 1300-1306

Kaplan D. M., Institute of Marine Sciences, https://pmc.ucsc.edu/~dmk/notes/EOFs/EOFs.html#Matlab_Code: [4 May, 2014]

Konotchick T., Parnell P.E., Dayton P.K., Leichter J.J., 2012, Vertical distribution of Macrocystis pyrifera nutrient exposure in southern California, *Estuarine, Coastal and Shelf Science*, 106, 85-92

Lentz S., Fewings M., 2012, The Wind- and Wave-Driven Inner-Shelf Circulation, *Annual Review of Marine Science*, 4, 317-343

Lentz S.J., Fewings M., Howd P., Fredericks J., Hathaway K., 2008, Observations and a Model of Undertow over the Inner Continental Shelf, *Journal of Physical Oceanography*, 38, 2341-2357

Lerczak J. A., Hendershott M. C., Winant C. D., 2001, Observations and modeling of coastal internal waves driven by a diurnal sea breeze, *Journal of Geophysical Research*, 106.C9, 19715-19729

Lerczak J. A., Winant C. D., and M. C. Hendershott, 2003, Observations of the semidiurnal internal tide on the southern California slope and shelf, *Journal of Geophysical Research: Oceans* (1978–2012), 108.C3, 3068

Lucas A., Franks P., Dupont C., 2011, Horizontal internal-tide fluxes support elevated phytoplankton productivity over the inner continental shelf, *Limnology and Oceanography: Fluids and Environments*, 1, 56–74

McPhee-Shaw E.E., Siegel D. A., Washburn L., Brzezinski M. A., Jones J. L., Leydecker A., Melack J., 2007, Mechanisms for nutrient delivery to the inner shelf: Observations from the Santa Barbara Channel, *Limnology and Oceanography*, 52(5), 1748–1766

Molina L., Pawlak G., Wells J., Monismith S., Merrifield M., 2014, Diurnal cross-shore thermal exchange on a tropical fore-reef, *Journal of Geophysical Research: Oceans*, 119, 6101-6120

National Center for Environmental Information, 2011, Magnetic Field Calculators, http://www.ngdc.noaa.gov/geomag-web/#declination [30 Jun, 2014]

National Center for Environmental Information, 2011, Quality Controlled Local Climatological Data, NCEI, NOAA, www.ncdc.noaa.gov/qclcd/QCLCD [15 Jan, 2015]

National Geophysical Data Center, 2003, U.S. Coastal Relief Model - Southern California, National Geophysical Data Center, NOAA[11 Nov, 2014]

Pawlowicz R., Beardsley B., Lentz S., 2002, Classical tidal harmonic analysis including error estimates in MATLAB using T_TIDE, *Computers and Geosciences*, 28, 929-937

Pineda J., 1999, Circulation and larval distribution in internal tidal bore warm fronts, *Limnology and Oceanography*, 44(6), 1400–1414

Rosman J. H., Koseff J. R., Monismith S. G., Grover J., 2007, A field investigation into the effects of a kelp forest (*Macrocystis pyrifera*) on coastal hydrodynamics and transport, *Journal of Geophysical Research*, 112, C02016

Shaffer R. L., 2007, Environment and Sustainability Initiative UC San Diego, Final Report, Metropolitan Wastewater Department, City of San Diego

Washburn L. and McPhee-Shaw E., 2013, Coastal transport processes affecting inner-shelf ecosystems in the California current system, *Oceanography*, 26, 34-43

Wilcox S., Andreas A., National Renewable Energy Laboratory, http://dx.doi.org/10.5439/1052230, [19 Mar, 2015]

Woodson B. C., 2013, Spatiotemporal Variation in Cross-Shelf Exchange across the Inner Shelf of Monterey Bay, California, *Journal of Physical Oceanography*, 43, 1648-1665